Supplementary Materials for

Pulvinar regulates information transmission between cortical areas based on attention demands

Yuri B. Saalmann[1,2*], Mark A. Pinsk[1,2†], Liang Wang[1,2†], Xin Li[1,2], Sabine Kastner[1,2]

*To whom correspondence should be addressed. Email: saalmann@princeton.edu

This PDF file includes:

Materials and Methods
Supplementary Text
Figs. S1 to S7
References (30-59)

Materials and Methods:

Behavioral Task

The Princeton University Animal Care and Use Committee approved all procedures, which conformed with the National Institutes of Health guidelines for the humane care and use of laboratory animals. We trained two male *Macaca fascicularis* monkeys (4-8 years old) to perform a variant of the Eriksen flanker task (*30*). Monkeys initiated trials by depressing a response lever after an auditory "go" tone. At trial onset, a small square fixation point (0.5°) appeared at the center of the monitor (eye-monitor distance = 57 cm). After a variable delay of 300-700 ms, a circular spatial cue randomly appeared (1.5°, 100 ms duration) at one of six possible stimulus locations. After another variable delay period of 400-800 ms, six barrel- or bowtie-shaped stimuli (each approximately 4x2°) appeared equally-spaced in a circular array around the fixation point, for 700 ms duration or until the monkey released the response lever. We positioned the circular array such that at least one stimulus appeared in the receptive field (RF) of recorded neurons (see "Electrophysiology" section below for RF mapping details). On half of the trials, the stimulus at the pre-cued location (target) was congruent with its nearest neighboring stimuli (distracters), that is, each of these three stimuli was barrel-shaped, or each was bowtie-shaped. On the other half of trials, the target and its nearest distracters were incongruent, that is, a barrel target was flanked by bowtie distracters, or vice versa. If a barrel appeared at the cued position, then the monkey needed to release the lever immediately for juice reward (150-650 ms after target onset). Conversely, if a bowtie appeared at the cued location, then the monkey needed to release the lever after the stimulus array disappears (150-650 ms after array disappearance). Because the number of barrels in the stimulus array equaled the number of bowties, random responses would be expected to produce a response accuracy of 50%. The monkeys performed the task with greater than 80% accuracy overall, suggesting that they attended to the cued location during the variable delay period until target presentation. To ensure that the monkey maintained fixation throughout each trial, the fixation point disappeared at a random time during 10% of trials, requiring the monkey to immediately release the lever (catch trials). We monitored eye position using an infrared eye tracker and trials were aborted if the monkey broke fixation, that is, if eye position deviated by more than one degree from fixation.

We controlled stimuli, response monitoring and rewards using Presentation software. Visual stimuli were presented at 50% contrast (light gray on darker gray background) on a 21 inch CRT monitor set at a refresh rate of 100 Hz. We verified visual stimulus timing using a customized photodiode system affixed to a second monitor receiving identical input. Monkeys reported decisions using a manual response lever and received juice reward delivered by an infusion pump. We monitored eye position using a stationary eye tracking system. We fed the video signal from an infrared camera (operating at 120 Hz) into an ASL eye-tracking processing unit, which interfaced with the experimental control computer running Presentation, in order to allow eye position feedback to influence trial outcomes.

Acquisition of Structural and Diffusion-Weighted Images

We anesthetized monkeys with Telazol (tiletamine/zolazepam, 10 mg/kg i.m.) and atropine (0.08mg/kg i.m.). During scan sessions, monkeys rested in a customized all-plastic MRI-compatible stereotaxic device. We monitored respiration rate and pulse rate using an MRI-compatible respiratory belt and pulse oximeter, respectively. We acquired images at a 3 T head-dedicated scanner using a 12-cm transmit-receive surface coil.

Prior to surgical implantation, we acquired diffusion-weighted images (DWI) using an eddy-current compensated double spin-echo, echo-planar pulse sequence (*31-33*). We collected images with 1.0 mm^2 in-plane resolution using 60 different isotropic diffusion directions (*34*) (field of view (FOV) = 128 x 96 mm; FOV phase = 75%; matrix = 128 x 96; phase partial fourier = 6/8; no. of slices = 47; slice thickness = 1.1 mm; repetition time (TR) = 10,000 ms; echo time (TE) = 145 ms; *b*-values = 0 and 1,000 s/mm^2; slice orientation = transverse). To improve the baseline SNR signal and to decrease the bias in tensor estimation, we increased the ratio of DWI to non-DWI acquired from the scanner default 60:1 ratio to a 12:1 ratio by collecting 5 non-DWI for each 60-direction set (*34, 35*). A total of twenty 60-direction sets of diffusion-weighted data were acquired for subsequent averaging. We acquired matching in-plane gradient echo field map and magnitude images to perform geometric unwarping of the DTI images (TR = 500 ms, TE = 6.53/8.99 ms, flip angle = 55°), as well as T1-weighted structural images for co-registration (Magnetization-Prepared RApid Gradient-Echo (MPRAGE); FOV = 128 mm^2; matrix = 256 x 256; no. of slices = 128; slice thickness = 0.5 mm; TR = 2,500 ms; TE = 4.38 ms; flip angle = 8°; inversion time (TI) = 1,100 ms; in-plane resolution = 0.5 mm^2). Total scan time for the DTI scan session was approximately 4 hours. To generate a higher quality structural brain image, we acquired 12 T1-weighted structural images in a separate scan session and calculated the mean image for each monkey.

Electrophysiology

All surgical procedures were performed under general anesthesia with isoflurane (induction 2–4%, maintenance 0.5– 2%) and under strictly aseptic conditions. We used titanium skull screws and dental acrylic to affix head implants on monkeys. Four 2.5 mm craniotomies were drilled within a customized plastic recording chamber, providing access to our pulvino-cortical regions of interest (ROIs) in the right hemisphere. We fitted each craniotomy with a conical plastic guide tube filled with bone wax (*36*), through which glass-coated platinum-iridium electrodes traversed. The wax-filled guide tubes held electrodes in place between recording sessions. During recordings, we stabilized the animal's head using four thin rods that slid into hollows in the side of the acrylic implants. We independently micropositioned electrodes in each ROI with electrode microdrives coupled to an adapter system allowing different approach angles for each ROI (that screwed onto the recording chamber). Electrode signals (40,000 Hz sample rate for spikes; 1,000 Hz sample rate for local field potentials (LFPs)) were amplified and filtered (150-8,000 Hz for spikes; 3-300 Hz for LFPs) using a preamplifier with a high input impedance headstage and Multichannel Acquisition Processor controlled by RASPUTIN software. We performed control recordings for LFP quality in each ROI with either a skull screw, silver wire in contact with the dura, or electrode in the white matter just outside the ROI, as the reference electrode. The LFPs recorded in a particular ROI remained similar across these control tests, so we used a skull screw as the reference electrode during recording sessions. We sorted spikes online to map the RF of isolated neurons and we re-sorted spikes for offline analyses using Plexon Offline Sorter software. We first hand-plotted a neuron's RF then confirmed the RF by systematically flashing visual stimuli around the RF location while the monkey fixated centrally. Pulvinar neurons in the overlap between V4 and TEO projection zones commonly had a RF around 5° in size. For each recording session, the RF overlap between recording sites was such that the circular 1.5° stimulus (cue) and one subsequent 4° x 2° stimulus evoked responses from each recording site. We also determined the neuron's preference for the barrel or bowtie stimuli that constituted the stimulus array. There were 51 recording sessions in total: 27 sessions with

monkey L, and 24 sessions with monkey C. Each recording session spanned a few hours of one day, with up to 5 sessions per week. We simultaneously recorded LFPs from the pulvinar, V4 and TEO in each of the 51 sessions (51 three-way LFP recordings). Across all recording sessions, we isolated 51 pulvinar neurons, 40 V4 neurons and 57 TEO neurons. The cortical neurons were sampled across the different layers of the cortex. For sessions in which an individual neuron could not be isolated from one of the ROIs, we used the multi-unit RF from that ROI to determine the RF overlap between recording sites.

DTI-Guided Electrode Positioning

Directly-connected cortical areas like V4 and TEO only connect with restricted, but overlapping zones in the pulvinar (*8*). To ensure neural recordings from inter-connected pulvino-cortical sites, we used DTI data to map probable paths between the pulvinar, V4 and TEO and targeted electrodes to the overlapping V4 and TEO projection zones in the pulvinar.

We used FSL software to analyze DTI data (*37, 38*). We corrected all DWI and non-DWI for eddy currents using affine registration (12 degrees of freedom (DOF), FMRIB's Linear Registration Tool (FLIRT)) to a non-DWI reference volume, and then averaged to improve the signal-to-noise ratio (*39*). After eddy current correction, we geometrically unwarped images using field map and magnitude images acquired in the same session (*40*). Briefly, the magnitude image was skull-stripped using FMRIB's Brain Extraction Tool (BET) (*41*), forward-warped using FMRIB's Utility for Geometrically Unwarping EPIs (FUGUE), and registered (6 DOF) to an averaged and skull-stripped non-DWI reference volume. The resulting transformation matrix was applied to the field map image (scaled to rad/s and regularized by a 2-mm 3D Gaussian kernel), which was subsequently used to unwarp all DWI and non-DWI using the FUGUE utility. We skull-stripped the T1-weighted structural image and co-registered to the averaged, skull-stripped and geometrically unwarped non-DWI reference volume (12 DOF) to derive the transformation matrix between the two spaces.

Using FMRIB's DTIFIT tool, we calculated diffusion tensors for each voxel using linear least squares fitting, and diagonalized to obtain the voxel eigenvalues and eigenvectors. We created fractional anisotropy (FA) maps and color maps of principle orientation to visually check for biologically plausible major fiber orientations across the entire brain before proceeding to perform probabilistic diffusion tractography (PDT) analyses (*42*).

We defined three ROIs for PDT analyses. ROIs of V4, TEO and the pulvinar were manually delineated for the right hemisphere of each animal. We used the individual monkey's brain anatomy from the T1-weighted structural image, in conjunction with a stereotaxic atlas, to guide the definition of the ROIs. The transformation matrix derived from the co-registration of the structural image to the reference non-DWI was applied to the ROI masks, which were visually inspected for proper alignment prior to PDT analyses.

We performed tractography analyses using FMRIB's Diffusion Toolkit (FDT). The tractography algorithm modeled two fiber populations per voxel (*43*), suited to the complex fiber architecture of the thalamus (*44*). For each monkey, we calculated probability distributions of fiber direction at each voxel using previously described methods (*44, 45*). First, to verify the anatomical plausibility of paths through the pulvinar and cortical ROIs, we performed a PDT analysis from each ROI to obtain the probable paths that pass through each ROI (i.e., FDT's "single mask

seed" tractography). The resulting pathways for each ROI were thresholded to remove voxels that contained less than 25 samples, and transformed back to the T1-weighted structural space of the monkey for viewing. We compared the trajectory of these pathways with results from previous tracer studies (e.g., *46*).

Second, we identified pulvinar voxels with a high probability of connection with V4 and TEO. We performed a PDT analysis to estimate pathways passing through any voxel in a pulvinar seed, and the probability such pathways will pass through a voxel in either of the two cortical targets, V4 and TEO (i.e., FDT's "single mask seed with classification targets" tractography). From each pulvinar seed voxel, 5000 samples were drawn from the probability distribution (0.2 curvature threshold, 0.25 mm step length), and the proportion of these samples passing through each cortical target equated to the probability of connection to that target. We calculated the overlap between pulvinar volumes respectively connected to V4 and TEO.

Finally, to determine probable paths between electrodes, we created a mask for each voxel in the structural image that contained an electrode tip (see below). The transformation matrix derived from the co-registration of the structural image to the reference non-DWI was applied to each mask, which were visually inspected for proper alignment prior to PDT analyses. We performed a PDT analysis to estimate paths that passed between a pair of electrode tip masks via a waypoint mask midway between electrode tips (i.e., FDT's "multiple masks" tractography; same PDT parameters as above).

To verify electrode locations in the pulvinar (generally, the lateral and inferior regions of the ventral pulvinar), V4 (prelunate gyrus) and TEO, we acquired T1-weighted structural images with platinum-iridium electrodes held *in situ* by customized guide tubes (*36*). While the actual electrode is not visible in the MR images, a susceptibility "shadow" artifact appears along the length of the electrode with a width of approximately one voxel (0.5 mm^3, either side of the electrode; Fig. S7). We targeted electrodes to interconnected pulvino-cortical ROIs based on the individual monkey's structural images and probabilistic tractography data, e.g., the zone within the pulvinar that has the highest probability of connecting with V4 and TEO (green zone in Fig. 1, B and C); a stereotaxic atlas (*47*) was used as a general reference. We re-positioned electrodes as necessary and re-acquired T1-weighted structural scans until electrodes were in their desired locations in the pulvinar and cortex. Our experimental approach was to position electrodes at the most dorsal point of an ROI (for a particular dorsal-ventral trajectory), then acquire structural images. During subsequent recording sessions, we microdrove electrodes through ROIs to isolate neurons and kept a record of electrode coordinates from the microdrive system for each session. At the end of an electrode track, i.e., at the most ventral point of our ROI, we acquired additional structural images, before starting a new track. We reconstructed electrode tracks as well as the position of the electrode for each recording session, using the structural images of the start and end of each track as well as the daily microdrive coordinates (conceptually, similar to re-constructing electrode tracks and recording sites in acute electrophysiology experiments).

Spike-Density Functions

We calculated spike density functions to measure the responses of pulvinar neurons. We convolved spikes from each trial with a Gaussian pulse (λ = 10 ms) and averaged the resulting functions to produce spike density diagrams for each neuron. To create population spike density functions, we normalized the spike rate for each neuron by its maximum response during trials,

then averaged the normalized rates of all neurons. We combined data from the two monkeys (for population spike density functions as well as spectral analyses) because their data was qualitatively similar. All data analyses included correct trials only. To compare attention conditions across the population, we used a *t* test to determine whether there was a significantly greater spike rate when attending to the RF versus attending away from the RF, for the delay period and for the presentation of the stimulus array.

Spike-Field Coherence

We calculated spike-field coherence using multi-taper methods (3 Slepian taper functions, time bandwidth product of 2) with the Chronux data analysis toolbox for Matlab (http://chonux.org/) (*48*, *49*). We used the coherence measure to study the temporal relationship between pulvinar spike trains and LFPs in the pulvinar, V4 and TEO. The coherence is given by $C(f) = S_{12}(f)/\sqrt{(S_{11}(f)S_{22}(f))}$, where S(f) is the spectrum with subscripts 1 and 2 referring to the simultaneously recorded spike train (pulvinar) and LFP (pulvinar, V4 or TEO). Different response rates do not affect the coherence (normalized between 0 and 1), so it can be averaged across different pairs of time series. For each paired recording from a pulvinar cell and LFP in either the pulvinar, V4 or TEO, we calculated the spike-field coherence in 300 ms sliding windows (50 ms steps across the trial) for each attention condition (e.g., attention at the RF location or attention away from the RF). The random location of stimuli from trial-to-trial result in attention conditions from any one recording session having an unequal number of trials. Because the number of trials affects the coherence estimate, we bias-corrected/transformed coherence values (*50*). The transformed spike-field coherence, T(f), is given by $T(f) = \tanh^{-1}(C(f))-1/(\nu_0-2)$, where ν_0 is the degrees of freedom; for our multi-taper estimates, $\nu 0 = 2*K*N$, where K is the number of tapers (3) and N is the number of trials. To obtain population values, we pooled the transformed coherence estimates. To control for spikes affecting the LFP, we excised 2 ms around each spike time from the raw data trace and linearly interpolated these segments of the data trace. Because the results of LFP analyses were the same regardless of whether spikes were excised or not (in the frequency range of interest), we reported LFP data without spike excision. For all spectral analyses, we mainly focused on the delay period after the evoked response until the array onset because therein the monkey maintained spatial attention and the data in each session generally satisfied methodological assumptions of stationarity (*51*). We tested whether the coherence was significantly above zero (*t* test, $p < 0.05$) in individual recording sessions using a jackknife estimate of the variance. To compare attention conditions across the population, we used *t* tests to determine whether there was significantly greater coherence in particular frequency bands (i.e., alpha and gamma) when attention was at the RF location compared to when attention was away from the RF. We controlled the experiment-wise error rate ($p < 0.05$) using the Holm's sequential Bonferroni procedure.

LFP-LFP Coherence

We also used the coherence measure to study the temporal relationship between LFPs in the pulvinar, V4, and TEO. We calculated LFP-LFP coherence using parametric methods with the BSMART toolbox for Matlab (*52*). We preprocessed the LFP from each brain area by bandpass filtering (3-100 Hz), downsampling to 200 Hz, subtracting the mean, then dividing by the standard deviation. For each recording session, we derived a multivariate autoregressive (MVAR) model for each attention condition (attention at the RF (response field for LFPs) corresponds to the location of the cue evoking the peak response; attention away from the RF corresponds to the location most far away in the opposite visual hemifield). The autoregressive

equation is given by $\sum_{m=0}^{p} A_m X(t-m) = E(t)$, where A_m are the coefficient matrices, m is the lag, $X(t)$ is the multidimensional process defined for a segment of the time series, and $E(t)$ is the noise vector. The model order, p, generally corresponded to the first minimum Akaike information criterion value. We used a model order of 10. To estimate A_m and V, the covariance matrix of the noise vector, we used the Levinson, Wiggins, Robinson algorithm. To check autoregressive models, we tested the assumption of white model residuals, the stability of the model (i.e., stationary and convergent), and the consistency between the recorded and model-generated data (*53*). The spectral matrix of the time series is given by $S(f) = H(f)VH^*(f)$, where $H(f) = (\sum_{m=0}^{p} A_m e^{-im2\pi f})^{-1}$ is the transfer function, and * denotes the matrix transpose and complex conjugate. The coherency is given by $C(f) = S_{ij}(f)/\sqrt{(S_{ii}(f)S_{jj}(f))}$, where S_{ij} is the $(i,j)^{th}$ element of S(f). We calculated the coherence in 200 ms, as well as 350 ms (to check low frequency results), sliding windows across the trial (results for the 200 ms analysis window shown in figures) and the analyses using each window size produced similar results. To cross-validate the multivariate-autoregressive-modeling-derived spectral results, we also calculated the multi-taper LFP-LFP coherence. Parametric (autoregressive) and nonparametric (multi-taper) coherence estimates produced similar results. For population statistics, we used *t* tests to determine whether there was significantly greater conditional Granger causality in particular frequency bands (e.g., alpha and gamma) when attention was at the RF location compared to when attention was away from the RF. We controlled the experiment-wise error rate ($p < 0.05$) using the Holm's sequential Bonferroni procedure.

Conditional Granger Causality

We calculated the conditional Granger causality (*54, 55*) as a measure of the influence one brain area (Y) has on another area (X), after taking into account additional areas (Z; core routines courtesy of Mingzhou Ding). The conditional Granger causality can be expressed as a function of frequency, to investigate the oscillatory nature of LFPs. In the frequency domain, the conditional Granger causality is given by $I_{Y\to X|Z}(f) = \ln \frac{\Sigma_{xx}(X,Z)}{|Q_{xx}(f)\hat{\Sigma}_{xx}(X,Y,Z)Q^*_{xx}(f)|}$, where $\Sigma_{xx}(X,Z)$ is the variance of the noise in the joint regression of X and Z (variance associated with X), and Q_{xx} and $\hat{\Sigma}_{xx}(X,Y,Z)$ are functions of the transfer function and noise covariance matrix (*56, 57*).

Similar to the preprocessing steps used for the parametric coherence estimates, we bandpass-filtered (3-100 Hz) the LFP from each brain area, downsampled to 200 Hz, subtracted the mean, then divided by the standard deviation. For MVAR modeling, we used a model order of 10, which generally corresponded to the first minimum Akaike information criterion value. For each attention condition (attention at the RF, and attention away from the RF), we calculated the conditional spectral Granger causality in 200 ms sliding windows, as well as 350 ms windows, across the trial (200 ms window results shown in figures), and the analyses using each window size produced similar results. We used a permutation test to determine whether there was significant conditional spectral Granger causality in individual recording sessions (*58*). This involved randomly shuffling the trial order of LFP data from each brain area and calculating the conditional spectral Granger causality on the shuffled data. Shuffling the trial order abolishes within-trial physiological interactions and produces Granger causality estimates due to chance. We repeated this procedure 1,000 times to generate a distribution of permutation estimates, and compared the actual Granger causality spectral peaks (derived from unshuffled data) to the distribution. To compare attention conditions across the population, we used *t* tests to determine whether there was significantly greater conditional Granger causality in particular frequency

bands (e.g., alpha and gamma) when attention was at the RF location compared to when attention was away from the RF. We controlled the experiment-wise error rate ($p < 0.05$) using the Holm's sequential Bonferroni procedure.

Cross-Frequency Coupling

Because low frequency oscillations have been shown to modulate high frequency activity (*18-20*), we used a cross-frequency coupling measure, the synchronization index (*59*), to study the interaction between alpha and gamma frequencies of the LFP in each cortical area. First, we extracted the power time series of the high frequency (gamma) activity. We bandpass-filtered detrended LFPs into bands with central frequencies from 20-100 Hz (in 5 Hz steps) and ± 5 Hz bandwidth. For each band, we obtained the power time series using the Hilbert transform.

Second, we extracted the lower frequency time series and transformed it to the frequency domain. We identified the frequency showing the highest power, in the range from 8 Hz to the bottom edge of the high frequency band. A frequency value between 8-15 Hz generally contained the highest power, and we bandpass-filtered the detrended LFPs with this central frequency and a bandwidth of ± 1.5 Hz.

Third, for each trial, we calculated the synchronization index in the 200 ms window during the delay period immediately before target presentation; we also used a 300 ms analysis window, which produced similar results (200 ms window results shown in figures). The synchronization index, SI, is given by $SI = \frac{1}{N}\sum_{t=1}^{N} e^{i[\emptyset_{lt} - \emptyset_{ut}]}$, where N is the number of time points, $\emptyset_{lt}$ is the phase value of the low-frequency (alpha band) time series, and $\emptyset_{ut}$ is the phase value of the high-frequency (gamma) power time series, at time point t. The magnitude of SI, SI_m, reflects the degree of phase synchrony. SI_m values range from zero to one: an SI_m of zero means phases are completely desynchronized; and an SI_m of 1 means phases are perfectly synchronized.

Finally, we used a boot-strapping technique to transform SI_m values to Z scores. We generated a distribution of SI_{mb} values by randomly shuffling the data 200 times. The normalized synchronization index, SI_Z, is given by $SI_Z = (SI_m - mean(SI_{mb}))/std(SI_{mb})$, where std is the standard deviation of the distribution of SI_{mb} values. We averaged SI_Z values across trials within a recording session. To compare attention conditions across the population, we applied a sign test on SI_Z to determine whether there was a significantly greater synchronization index (alpha modulating gamma (30-60 Hz)) when attention was at the RF location compared to when attention was away from the RF.

Supplementary Text

There was also evidence for cortical influence on the pulvinar during the delay period, in addition to the robust influence of the pulvinar on the cortex (Fig. 4). Due to the space limitations on the main text, we discuss the cortico-pulvinar influence below.

Cortical Influence on the Pulvinar

Because the cortex provides the major input to the pulvinar, it is likely that necessary information for the pulvinar to determine attentional priorities and maintain their representation derives largely from the cortex. Figure S6, A and B, respectively show the influence of V4 and

TEO on the pulvinar, for all sessions. There was significantly greater V4-to-pulvinar and TEO-to-pulvinar influence in the 3-7 Hz (theta) range with attention at the RF location versus attention away from the RF (Holm's controlled *t* tests, $p < 0.05$), suggesting visual cortex as a source of information about the cued location for the pulvinar.

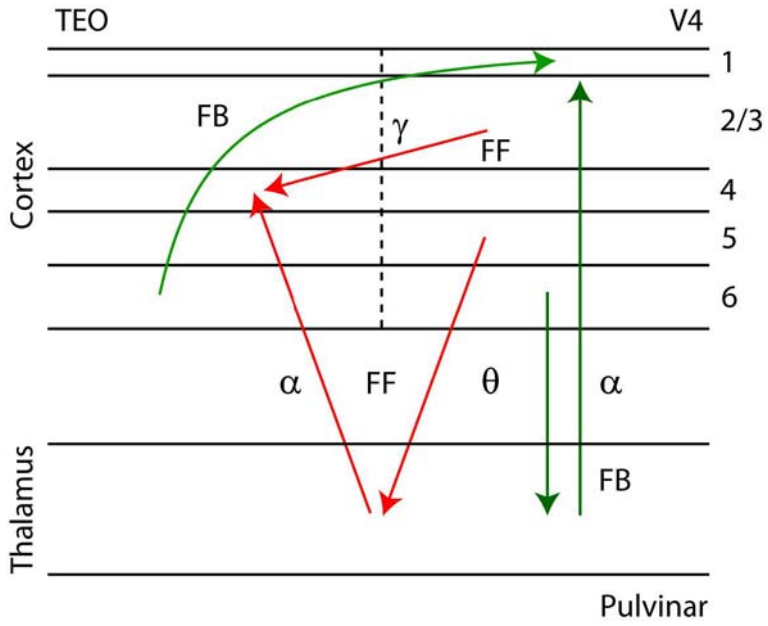

Fig. S1. Pulvino-cortical connectivity schematic. Direct cortico-cortical connections (top) and indirect cortico-pulvino-cortical loops exemplified by V4-pulvino-TEO circuitry. Our results suggest frequency-band-specific influences for different circuit paths. The pulvinar first increased synchrony between cortical areas after the spatial attention cue, and this cortical synchrony was maintained throughout the delay period and presentation of the target. The pulvinar predominantly influenced the cortex in the alpha frequency range. Through cross-frequency coupling, the pulvinar-controlled alpha oscillations modulated gamma frequency activity in the cortex, contributing to the inter-areal coherence in gamma activity (observed in addition to alpha coherence). When the target appeared amid distracters, the pre-established cortical synchrony served to enhance transmission of the behaviorally relevant visual information. Red, feedforward pathways; green, feedback pathways.

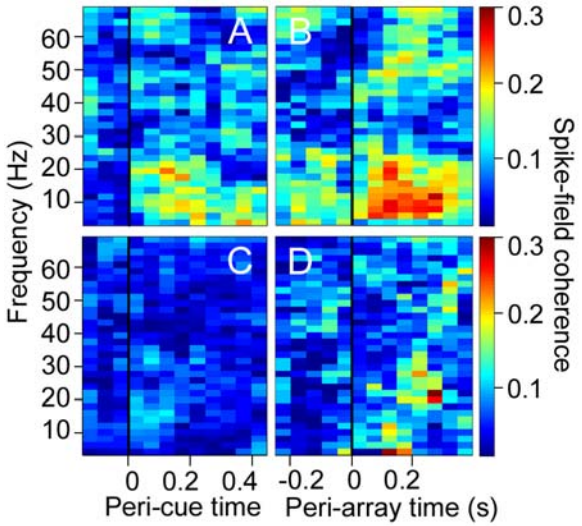

Fig. S2. Attention modulated neural synchrony in the pulvinar. **(A-D)** Pulvinar spike-field coherence (color-coded) for a typical session, calculated in successive 300 ms windows with a step size of 50 ms. **(A)** Cue and **(B)** target at RF. **(C)** Cue and **(D)** target away from RF. Same stimuli presented in (B) and (D).

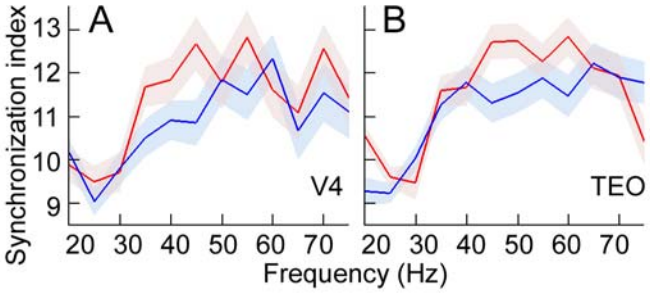

Fig. S3. Attention modulated cross-frequency coupling between alpha and gamma oscillations in the cortex. Population normalized (Z-scored) synchronization index (±SE) for **(A)** V4 and **(B)** TEO, calculated in the 200 ms window prior to target onset. Red, attention at the RF; blue, attention away from the RF.

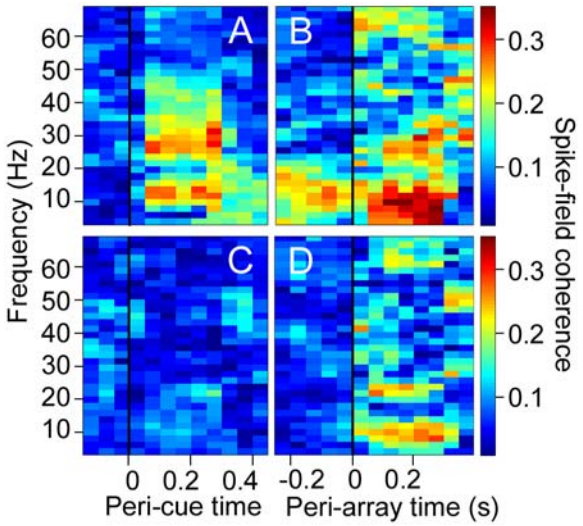

Fig. S4. Attention modulated the synchrony between the pulvinar and TEO. **(A-D)** Coherence (color-coded) between pulvinar spikes and TEO LFP for a typical session, calculated in successive 300 ms windows with a step size of 50 ms. **(A)** Cue and **(B)** target at RF. **(C)** Cue and **(D)** target away from RF. Same stimuli presented in (B) and (D).

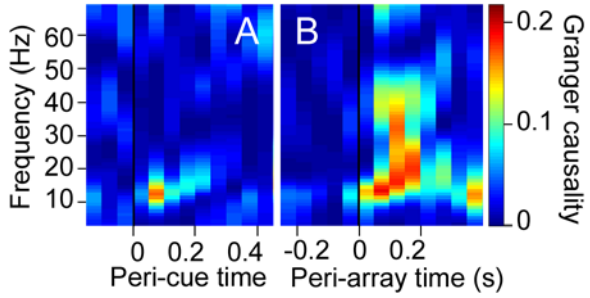

Fig. S5. Weak cortico-cortical influences during the delay period in the absence of visual stimulation. Conditional Granger causality (color-coded) from V4 to TEO (accounting for the pulvinar) for a typical session, calculated in successive 200 ms windows with a step size of 50 ms. **(A)** Cue and **(B)** target at RF.

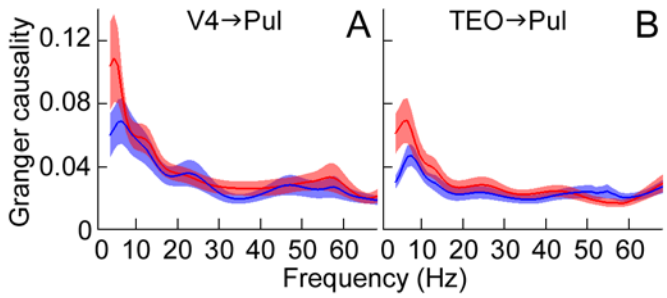

Fig. S6. Attention modulated cortico-pulvinar influences in the theta frequency range. Population average of the conditional Granger causality for **(A)** V4 influence on the pulvinar, and **(B)** TEO influence on the pulvinar, calculated in the 200 ms window prior to target onset. Red, attention at the RF; blue, attention away from the RF.

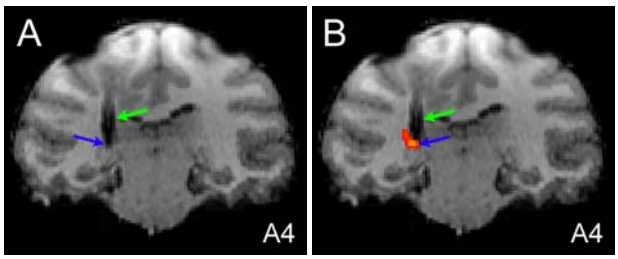

Fig. S7. Probable path from TEO electrode terminating at pulvinar electrode tip. **(A)** Structural MRI scan shows pulvinar electrode position for one recording session. **(B)** DTI data overlaid on the same slice shown in (A). Probable path colored red-yellow. Green arrow points to the "shadow" around the electrode shaft and the blue arrow points to the electrode tip. Electrode track angles slightly from posterior to anterior. "Shadow" on cortical surface from nearby skull screws. Fig. 1F shows corresponding coronal slice from high quality structural brain image (mean of 12 T1-weighted images) with the same DTI data overlaid.

References and Notes for Supplementary Materials

30. C. W. Eriksen, The Flankers Task and Response Competition: A Useful Tool for Investigating a Variety of Cognitive Problems. *Visual Cognition* **2**, 101-118 (1995).
31. P. L. Croxson *et al.*, Quantitative investigation of connections of the prefrontal cortex in the human and macaque using probabilistic diffusion tractography. *J. Neurosci.* **25**, 8854-8866 (2005).
32. N. Ramnani *et al.*, The evolution of prefrontal inputs to the cortico-pontine system: diffusion imaging evidence from Macaque monkeys and humans. *Cereb. Cortex* **16**, 811-818 (2006).
33. T. G. Reese, O. Heid, R. M. Weisskoff, V. J. Wedeen, Reduction of eddy-current-induced distortion in diffusion MRI using a twice-refocused spin echo. *Magn. Reson. Med.* **49**, 177-182 (2003).

34. D. K. Jones, M. A. Horsfield, A. Simmons, Optimal strategies for measuring diffusion in anisotropic systems by magnetic resonance imaging. *Magn. Reson. Med.* **42**, 515-525 (1999).
35. T. Zhu, X. Liu, P. R. Connelly, J. Zhong, An optimized wild bootstrap method for evaluation of measurement uncertainties of DTI-derived parameters in human brain. *Neuroimage* **40**, 1144-1156 (2008).
36. I. N. Pigarev, Y. B. Saalmann, T. R. Vidyasagar, A minimally invasive and reversible system for chronic recordings from multiple brain sites in macaque monkeys. *J. Neurosci. Methods* **181**, 151-158 (2009).
37. S. M. Smith *et al.*, Advances in functional and structural MR image analysis and implementation as FSL. *Neuroimage* **23 Suppl 1**, S208-219 (2004).
38. M. W. Woolrich *et al.*, Bayesian analysis of neuroimaging data in FSL. *Neuroimage* **45**, S173-186 (2009).
39. M. Jenkinson, S. Smith, A global optimisation method for robust affine registration of brain images. *Med. Image Anal.* **5**, 143-156 (2001).
40. P. Jezzard, R. S. Balaban, Correction for geometric distortion in echo planar images from B0 field variations. *Magn. Reson. Med.* **34**, 65-73 (1995).
41. S. M. Smith, Fast robust automated brain extraction. *Hum. Brain Mapp.* **17**, 143-155 (2002).
42. S. Mori, P. B. Barker, Diffusion magnetic resonance imaging: its principle and applications. *Anat. Rec.* **257**, 102-109 (1999).
43. T. E. Behrens, H. J. Berg, S. Jbabdi, M. F. Rushworth, M. W. Woolrich, Probabilistic diffusion tractography with multiple fibre orientations: What can we gain? *Neuroimage* **34**, 144-155 (2007).
44. T. E. Behrens *et al.*, Non-invasive mapping of connections between human thalamus and cortex using diffusion imaging. *Nat. Neurosci.* **6**, 750-757 (2003).
45. T. E. Behrens *et al.*, Characterization and propagation of uncertainty in diffusion-weighted MR imaging. *Magn. Reson. Med.* **50**, 1077-1088 (2003).
46. J. D. Schmahmann, D. N. Pandya, *Fiber pathways of the brain*. (Oxford Univ. Press, New York, 2006).
47. K. S. Saleem, N. Logothetis, *A combined MRI and histology atlas of the rhesus monkey brain in stereotaxic coordinates*. (Academic, Burlington, MA, 2007).
48. H. Bokil, P. Andrews, J. E. Kulkarni, S. Mehta, P. P. Mitra, Chronux: a platform for analyzing neural signals. *J. Neurosci. Methods.* **192**, 146-151 (2010).
49. P. Mitra, H. Bokil, *Observed brain dynamics*. (Oxford Univ. Press, New York, 2008).
50. H. Bokil, K. Purpura, J. M. Schoffelen, D. Thomson, P. Mitra, Comparing spectra and coherences for groups of unequal size. *J. Neurosci. Methods* **159**, 337-345 (2007).
51. M. R. Jarvis, P. P. Mitra, Sampling properties of the spectrum and coherency of sequences of action potentials. *Neural Comput.* **13**, 717-749 (2001).
52. J. Cui, L. Xu, S. L. Bressler, M. Ding, H. Liang, BSMART: a Matlab/C toolbox for analysis of multichannel neural time series. *Neural Netw.* **21**, 1094-1104 (2008).
53. M. Ding, S. L. Bressler, W. Yang, H. Liang, Short-window spectral analysis of cortical event- related potentials by adaptive multivariate autoregressive modeling: data preprocessing, model validation, and variability assessment. *Biol. Cybern.* **83**, 35-45 (2000).

54. J. F. Geweke, Measures of Conditional Linear-Dependence and Feedback between Time-Series. *J. Am. Stat. Assoc.* **79**, 907-915 (1984).
55. C. W. J. Granger, Testing for Causality - a Personal Viewpoint. *J. Econ. Dyn. Control* **2**, 329-352 (1980).
56. M. Ding, Y. Chen, S. L. Bressler, in *Handbook of time series analysis: recent theoretical developments and applications,* B. Schelter, M. Winterhalder, J. Timmer, Eds. (Wiley-VCH, Weinheim, 2006), pp. 437-460.
57. M. Dhamala, G. Rangarajan, M. Ding, Analyzing information flow in brain networks with nonparametric Granger causality. *Neuroimage* **41**, 354-362 (2008).
58. A. Brovelli *et al.*, Beta oscillations in a large-scale sensorimotor cortical network: directional influences revealed by Granger causality. *Proc. Natl. Acad. Sci. U. S. A.* **101**, 9849-9854 (2004).
59. M. X. Cohen, Assessing transient cross-frequency coupling in EEG data. *J. Neurosci. Methods* **168**, 494-499 (2008).